Showcasing research from Professor Sun's laboratory, University of Hawaii, USA.

Trifluoroacetic acid formation from HFC-134a under atmospheric conditions

Trifluoracetic acid (TFA) has long been considered a primary product of atmospheric oxidation of hydrofluoric refrigerants like HFC-134a. TFA poses a significant environmental challenge due to its extreme persistence and irreversible accumulation in water, soil, and even living organisms. While global atmospheric models employ speculative reaction pathways of forming TFA from HFC-134a, many proposed reactions lack theoretical foundation. This study outlines the potential energy profile of atmospheric radicals reacting with HFC-134a and subsequent reactions that form TFA. Kinetics studies suggests that neither TFA nor its precursor trifluoroacetyl fluoride (TFAF) could be formed *via* these speculative reaction pathways.

Image reproduced by permission of Rui Sun from *Phys. Chem. Chem. Phys.*, 2026, **28**, 4433.

As featured in:

See Rui Sun *et al.*, *Phys. Chem. Chem. Phys.*, 2026, **28**, 4433.

PCCP

ROYAL SOCIETY OF CHEMISTRY

PAPER

View Article Online
View Journal | View Issue

Cite this: *Phys. Chem. Chem. Phys.*, 2026, **28**, 4433

Trifluoroacetic acid formation from HFC-134a under atmospheric conditions

Allen Vincent, Kazuumi Fujioka, Yuheng Luo, Ralf Kaiser and Rui Sun *

Trifluoracetic acid (CF_3COOH, TFA) is touted as a primary degradation product from atmospheric oxidation of HFC-134a (CF_3CH_2F). TFA poses a significant environmental challenge, such as bioaccumulation due to its high stability in terrestrial conditions. While several global atmospheric modeling studies predict varied amount of TFA formed from HFC-134a, the potential energy profile of this process has not been established and many of the proposed reaction mechanisms remain at the level of pushing arrows. This theoretical study first outlines the potential energy profile of OH radical initiated oxidation of HFC-134a along with subsequent reactions that lead to the formation of TFA. Secondly, master equation simulations are performed to quantify the kinetics of each reaction step mimicking atmospheric conditions. Key findings from the potential energy profile reveal detailed mechanism involved in TFA formation along with other competing fluorinated products. However, both TFA and its precursor trifluoroacetyl fluoride (CF_3CFO, TFAF) product forming channels have inaccessible energy barriers under atmospheric conditions. Although this research does not rule out the possibility that TFA can be formed from HFC-134a in the atmosphere, it casts doubt on the feasibility of the previous proposed mechanism.

Received 1st September 2025,
Accepted 25th November 2025

DOI: 10.1039/d5cp03359d

rsc.li/pccp

Introduction

Hydrofluorocarbons (HFCs) are the third generation of refrigerants when chlorofluorocarbons (CFCs) were identified as the main cause of ozone depletion in the 1980s.[1] Since the early 1990s, HFCs have been found to be a suitable replacement for CFCs in accordance with the Montreal protocol.[2] While the ozone depletion problem was resolved by replacing CFCs with HFCs, the relatively long tropospheric lifetime and high global warming potential of HFCs have raised concerns about its large-scale application on the commercial scale. In addition, a more nuanced consequence of HFCs is their potential contribution to the formation of per- and polyfluoroalkyl substances (PFAS) after they are released into the atmosphere. PFAS are chemically stable, persistent to environmental degradation, and can accumulate in living organisms. PFAS exposure has been linked to a range of health issues, including reproductive problems, developmental delays, increased cholesterol, immune system dysfunction, and an increased risk of certain cancers.[3] One such molecule being touted as a major degradation product of HFCs in the atmosphere is trifluoroacetic acid (TFA, CF_3COOH). TFA is highly soluble in water with a pK_a value of 0.47.[4,5] TFA has an atmospheric lifetime of up to 230 days with respect to OH radicals.[6–8] There is little to no knowledge of its degradation pathways in the environment and it is considered to be a persistent chemical that accumulates in aquatic biospheres and soil samples.

HFC-134a (CF_3CHF_2) remains widely used in automotive air conditioning, commercial refrigeration, and medium-temperature chillers due to its favorable thermodynamic properties and zero ozone depletion potential.[9–11] First reported by Wallington *et al.* in 1996, HFC-134a is one of the refrigerant molecules that has been proposed as one of the initial precursors for TFA formation.[12] This report argues 7–20% of HFC-134a is estimated to form trifluoroacetaldehyde fluoride (TFAF, CF_3COF) in the atmosphere, which further undergoes hydrolysis to form TFA. Franklin presents one of the earliest full-scale degradation of HFC-134a in the atmosphere to form TFA formation in both the gas- and condensed-phase.[13] The amount of TFA formed from atmospheric breakdown of HFC-134a was first estimated to be ~80 nM by Ball *et al.*[14] Precipitation brings TFA to the surface of earth, where Kanakidou *et al.* estimated 1 nM of TFA in rainwater with global atmospheric modelling of the life cycle of HFC-134a in the troposphere.[15] Wu *et al.* sampled the atmospheric concentration of TFA in Beijing, China and estimated the deposition flux using a deposition model.[16] According to this study, about 14% of the TFA is formed from degradation of HFC-134a, which indicates other possible major sources of TFA. In another global atmospheric modeling of the hydrolysis and precipitation of TFA, Luecken *et al.* estimated the TFA formation from HFC-134a to

Department of Chemistry, University of Hawai'i at Manoa, Honolulu, Hawaii 96822, USA. E-mail: ruisun@hawaii.edu

be close to 21%.[17] Jordan *et al.* conducted field observations in Germany in the duration but found when a substantial increase in atmospheric HFC-134a was observed, no significant increase in TFA concentration in the precipitation for as long as one year.[18] There are other studies even reporting up to 90% of TFA formation from HFC-134a.[19–23] The wide predicted range fuels speculations about how much TFA is formed from HFC-134a.

The degradation of HFC-134a starts with its oxidation by radicals in the atmosphere like $O(^1D)$, OH and Cl, and each have been extensively studied in literature since the 1990s.[24–29] Since OH radical is the most abundant among the three, the widely accepted first step of the reaction is $CF_3CH_2F + OH \rightarrow CF_3CHF + H_2O$, where the H atom from HFC-134a is abstracted by the radical. Clyne *et al.* reported the first rate constant of the reaction ($k = (5.5 \pm 0.7) \times 10^{-15}$ cm^3 molecule^{-1} s^{-1} at 295 K) with a flow tube experiment.[30] This study was followed by a series of experiments, where although the details are different, the reported rate constant were all on the order of 10^{-15} cm^3 molecule^{-1} s^{-1} within the temperature range between 220 K to 300 K.[24,28,31–33] Regarding the subsequent reaction of CF_3CHF radical to TFA or its precursor TFAF, O_2 addition to form CF_3CHFO_2 peroxy radical has been regarded as the most probable.[34] The lifetime of the peroxy radical has been measured to be $\sim$100 s in the atmosphere, which makes it feasible to react with other reactive radicals. Some example rate constants for the reaction of CF_3CHFO_2 peroxy radicals with atmospheric radicals are: $k(CF_3CHFO_2 + HO_2) = (4.0 \pm 0.2) \times 10^{-12}$ cm^3 molecule^{-1} s^{-1} at 296 $\pm$ 2 K, $k(CF_3CHFO_2 + NO_2) = (5.0 \pm 0.5) \times 10^{-12}$ cm^3 molecule^{-1} s^{-1} at 296 $\pm$ 2 K and $k(CF_3CHFO_2 + NO) = (1.28 \pm 0.36) \times 10^{-11}$ cm^3 molecule^{-1} s^{-1} at 298 K.[35–39]

By piecing the aforementioned studies (*e.g.*, the H atom abstraction, O_2 addition, and further decomposition) together, one can draw the current knowledge of the degradation pathway of HFC-134a in the atmosphere. However, a full-scale potential energy profile reflecting such knowledge, starting from the OH radical addition to HFC-134a to the formation of TFA, is yet to be established. In fact, none of these studies reported the energetics or the mechanism (*e.g.*, what are the intermediates and rate-limiting steps involved) of these proposed reactions. Such information is of fundamental importance to understand the fate of refrigerant molecules in the atmosphere, which together, will shed light on predicting the potency of novel refrigerant molecules in forming TFA and other PFAS molecules. In this manuscript, we employ HFC-134a as an example and examine its proposed degradation in the atmosphere to form TFA. First, we provide an accurate potential energy profile to understand the reaction mechanisms and energetics involved. Second, we quantify the kinetics of these reactions at different temperatures and pressures that are relevant to atmospheric conditions. Together, we explore the most energy-efficient pathway and analyze whether HFC-134a has largely contributed to TFA's formation in the atmosphere. It is also important to note that since there are a large number of radical molecules in the atmosphere and there are other fundamentally different reaction pathways (*e.g.*, photochemistry, reactions in aerosol and ice grains, *etc.*), it is impossible for any single study, including ours, to consider all possible reactions of HFC-134a.

Methodology

Potential energy profile

The density functional theory (DFT) calculations reported in this work are carried out with NWChem 7.2.[40] The geometry optimizations are performed using the M06-2X-D3 functional and cc-pVTZ basis set for all atoms.[41,42] To account for long-range, non-covalent correlation effects such as van der Waals interactions, an empirical potential such Grimme's D3 dispersion correction is added to the DFT energies.[43,44] The identity of the stationary points is confirmed by performing frequency calculations. $3N$-6 vibrational modes correspond to the reactants, products, intermediates and $3N$-7 vibrational modes correspond to the transition states, where N is the number of atoms in the species. Transition states connecting pairs of intermediates are confirmed using intrinsic reaction coordinate (IRC) calculations.[45] Considering the large amount species to be identified in this research, M06-2X-D3/cc-pVTZ is selected for its efficiency in exploring the configurational space and finding optimal geometries.[41,46–50] Although diffuse functions are generally necessary for best performance,[51] they were excluded because the marginal gain in accuracy for the reactions examined did not justify the increased computational cost as shown in Table T1 in the SI. The potential energy of these optimal geometries is further refined with the cc-pVTZ-F12 basis set and coupled cluster with single and double excitations and perturbative triples with explicitly correlated F12 method (CCSD(T)-F12).[52–54] These CCSD(T)-F12 calculations were carried out with ORCA 5.0.[55] The hybrid method, CCSD(T)-F12/cc-pVTZ-F12//M06-2X-D3/cc-pVTZ, has shown to be accurate in similar radical systems.[56]

Pressure dependent kinetics

MultiWell-2023.1 program suite is employed to calculate rate constants and product fractional yields based on the Rice–Ramsperger–Kassel–Marcus (RRKM) theory.[57,58] The inputs for MultiWell are the potential energy (CCSD(T)-F12/cc-pVTZ-F12) and vibrational frequencies (M06-2X-D3/cc-pVTZ) of the reactants, products, intermediates, and transition states. MultiWell uses this information to compute the sums and densities of states with the densum module. The ktools module calculates the microcanonical variational transition state theory rate (VTST) constants for barrierless association/dissociation for a collection of points along the reaction coordinate.[59,60] The density of states is calculated up to E_{max} = 60 000 cm^{-1} with an energy grain ΔE_{grain} = 50 cm^{-1} to account for the highest reaction energy threshold. The lower energy domain of each state is accounted by using ΔE_{grain} = 5 cm^{-1} with 801 grain counts leading up to 4000 cm^{-1} which is well above the vibrational frequency of any mode in the current reaction system. N_2 is used as the colliding medium, and the collision

energy transfer is described by the single exponential-down model with average transfer energy function:[61]

$$\langle E_d \rangle = \exp(-(E - E_0)/\alpha(E))$$

where, $\alpha(E) = 39.3 + (0.0159 \times E) - (2.63 \times E^2)$ estimated by Schneider *et al.* for an analogous system CF_3CFHO colliding with N_2 gas.[62] The spin–orbit coupling energies and degeneracies of OH and NO radicals are accounted for in the RRKM electronic partition function. The tunneling corrections for transition states are accounted for based on an unsymmetrical Eckart barrier within the MultiWell program.

Results and discussion

OH radical initiated oxidation of HFC-134a

The potential energy profile at doublet state for the OH radical and HFC-134a bimolecular reaction is shown in Fig. 1 with four bimolecular product channels being: (i) hydrogen abstraction channel forming CF_3CHF radical and H_2O (**p1**, −15.1 kcal mol^{-1}), (ii) the H atom loss channel forming CF_3CHFOH and H atom (**p2**, −4.2 kcal mol^{-1}), (iii) C–C bond fission leading to formation of CF_3OH and CH_2F radical (**p3**, −17.7 kcal mol^{-1}), and (iv) C–C bond fission leading to the formation of CFH_2OH and CF_3 radical (**p4**, −4.3 kcal mol^{-1}). For discussion purposes the carbon of CF_3 group in CF_3CH_2F is labelled as C1 and the carbon of CH_2F group is labelled as C2. The barrierless association of OH and CF_3CHF_2 (**r**) leads to the van der Waals (vdW) complex **i1** which is −4.0 kcal mol^{-1} with respect to **r**.

i1 serves as the complex which has access to the rest of the potential energy profile *via* three energy barriers. First, **i1** can go through a shallow transition state **ts-1-2** (2.3 kcal mol^{-1}) connecting to **i2** (−17.8 kcal mol^{-1}), where the H atom facing the radical is abstracted by the OH radical. **i2**, a hydrogen bond complex, can undergo barrierless dissociation to form **p1** ($CF_3CHF + H_2O$). **i2** can also form **p2** (CF_3CHFOH + H) *via* a steep energy barrier **ts-2-p2** (46.4 kcal mol^{-1}), where the O atom of the water molecule approaches the C2 atom, forms the O–C2 bond, and pops out an H atom. Second, **i1** can go through a high transition state **ts-1-p2** (54.2 kcal mol^{-1}) to also form product **p2**. This pathway is similar to the S_N2 reaction mechanism where the OH radical approaches the sterically less hindered C2 carbon, therefore distorting the tetrahedral bonding geometry of C2 atom which leads to the substitution of one of the H atoms by the OH radical. Last, **i1** connects to another high transition state **ts-1-3** (68.8 kcal mol^{-1}). The weakened tetrahedral bonding geometry of C2 atom (see the previous pathway) leads to the dissociation of the C1–C2 bond. The resulting species form a vdW complex **i3** ($[CF_3OH \cdots CH_2F]$, −21.1 kcal mol^{-1}), which could directly dissociate in a barrierless process to form **p3** ($CF_3OH + CH_2F$ radical). Alternatively, the –OH group in **i3** could be shuffled from C1 to C2 *via* transition state **ts-3-4** (39.2 kcal mol^{-1}) to form a vdW complex **i4** ($[CF_3 \cdots CH_2FOH]$, −6.2 kcal mol^{-1}). Similar to **i2** and **i3**, **i4** can dissociate barrierlessly to form **p4** (CF_3 + CH_2FOH). **i4** also has access to product **p2** *via* a high transition state **ts-4-p2** (51.6 kcal mol^{-1}), where the C1 and C2 species recombine, weakened the tetrahedral bonding geometry of C2 atom, and lead to the dissociation of C2–H bond to form a Hydrogen loss product (**p2**).

Although all four products in Fig. 1 have lower energy than the reactant, forming them (except **p1**) involves overcoming significant barriers. Considering the low temperature in the atmosphere (210–300 K, corresponding to 0.6–0.9 kcal mol^{-1} collision energy), the barrierless dissociation pathway of **i2**, **i3**, and **i4** should be favored over the isomerization pathway and **p1** should be the predominant product. The more intriguing question is once **i1** is formed as a result of the exothermal association of HFC-134a and OH radical (**r**), both of which are present in the atmosphere, is **i1** long-lived enough to form **p1**,

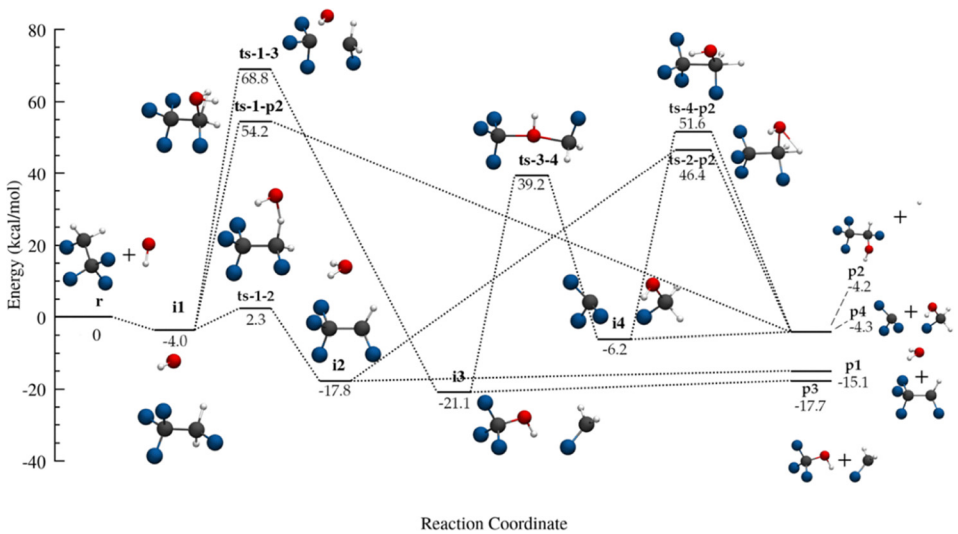

Fig. 1 Potential energy profile of the CF_3CH_2F (HFC-134a) + OH reaction computed with CCSD(T)-F12/cc-pVTZ-F12//M06-2X-D3/cc-pVTZ level of theory with ZPE included. The atoms are represented as black (C), blue (F), red (O) and white (H).

which involves larger configurational change, or does it simply dissociate back to **r**. Herein we employ the master equation simulations to mimic relevant temperatures and pressures of the troposphere to unravel the fate of **i1**.

The master equation simulation is initiated from **i1** with a temperature range of 210–300 K and a pressure range of 0.05–1.0 bar, corresponding to the altitude between sea level and ~17 km above sea level (the tropopause). The Lennard-Jones (LJ) parameters for HFC-134a (σ_1 = 3.82 Å, ε_1 = 140.4 K) and OH radical (σ_2 = 3.05 Å, ε_2 = 56.8 K) is used to obtain the LJ parameters for the intermediates **i1** and **i2** using the following combination expressions, $\sigma_i = (\sigma_2 + \sigma_2)/2$ and $\varepsilon_i = \sqrt{\varepsilon_1 \times \varepsilon_2}$.[63,64] The LJ parameters for N_2 (σ = 3.70 Å, ε = 84.9 K) as bulk gas is employed in the master equations. The results indicate that none of the transition states except **ts-1-2** are energetically accessible under the simulated atmospheric condition and the only populated outcome is the hydrogen abstraction product, **p1**, and the dissociated reactants, HFC-134a + OH (**r**). Therefore, the reaction pathway **r** ↔ **i1** ↔ **ts-1-2** ↔ **i2** ↔ **p1** is the focus of the kinetics study, where all steps along the pathway are considered to be reversible. The fraction of **p1** formed from **i1** is plotted in Fig. 2 at various temperatures and pressures. The dotted line represents the temperature-pressure trendline with increasing altitude in the troposphere. At room temperature and ambient pressure (*e.g.*, sea level), **p1** is barely formed and most of the **i1** dissociates back to the reactants. As the altitude increases (*e.g.*, the temperature and pressure decreases), more **p1** forms. For example, at 0.1 atm and 210 K (altitude: ~17 km), 42% of the **i1** goes through the aforementioned reaction path and form **p1**.

This interesting trend prompted an analysis of the vibrational energy of remaining **i1** and yield of **r** and **p1** as a function of time. Herein we focused on the upper and lower limit of temperature and pressure (300 K and 1.0 atm; 210 K and 0.1 atm) in Fig. 3. Note at the beginning of the simulation (t = 0), the vibrational energy (E_{vib}) of **i1** includes the ZPE (E_{ZPE}, 36.4 kcal mol^{-1}), the thermal vibrational excitation sampled at corresponding temperature (E_T), and the potential energy release from the association of HFC-134a and OH radical (E_P, 4.0 kcal mol^{-1}). E_T is sampled from a Boltzmann distribution. After the simulation starts, the fraction of **i1** with large E_{vib} predominantly dissociates to form the reactants (**r**, 4.0 kcal mol^{-1} above **i1**). The fraction is higher at 300 K (47%) compared to 210 K (10%), as there is a larger portion of **i1** possessing enough energy to dissociate to **r**. At the beginning of the simulation, the fraction of **i1** that can access **ts-1-2** (6.3 kcal mol^{-1} above **i1**) is negligible (2.9% and 0.3% for 300 K and 210 K, respectively), thus **i2** and **p1** are not formed. Once the vibrationally excited **i1** is eliminated, the depletion rate of **i1** fraction slows down. The reaction only takes place when **i1** is excited through collisions with N_2 bath gas, which forms either **r** or cross **ts-1-2** to form **i2**. Since **i2** is only 2.6 kcal mol^{-1} lower than the dissociated species **p1**, the excess energy released from **ts-1-2** makes it short-lived (*i.e.*, steady-state approximation) thus its fraction is on the order of 10^{-5} and not visible in Fig. 3. The N_2 collision activation makes those **i1** molecules possessing relatively high energy react first, thus the vibrational energy of remaining **i1** (red line) keeps decreasing, until all of the species are eliminated. Here, we stop tracking the vibrational energy of the remaining **i1** once its fraction drops below 0.1% to avoid large fluctuations. A lower pressure (dashed line, P = 0.1 atm) elongates the process as the N_2 collision activation is less frequent, but it does not fundamentally change how the species evolve. The simulation shows that **p1** can be formed from HFC-134a at high altitudes in the troposphere, which is supported by the experimental and/or global atmospheric modeling studies where CF_3CHF is the only product being formed in this step. It is also interesting to note that tunneling plays an important role in forming **p1**, as the simulation without the tunneling effects results in 100% of **i1** going back to **r**. From now on, the analysis of the manuscript will focus on the further degradation of CF_3CHF radical in the atmosphere and disregard the rest of potential products in Fig. 2.

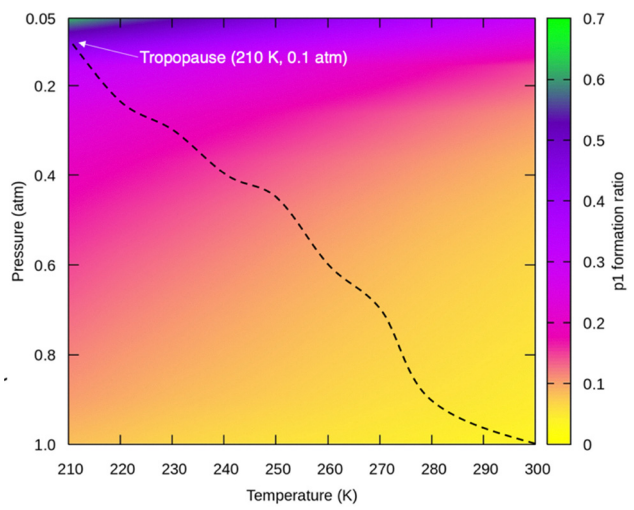

Fig. 2 Fraction of p1 formed as a function of temperature and pressure. The dotted line represents the temperature and pressure trend with altitude increase in the troposphere, starting from T = 300 K and P = 1 atm at sea level to T = 210 K and P = 0.1 atm at 18 km (tr).

O_2 addition to CF_3CHF radical

CF_3CHF radical has been hypothesized to undergo further degradation through reaction with O_2 ($^3\Sigma_g^-$) in the atmosphere but the energetics of these reactions have not been reported.[34] Since DFT is prone to misrepresent reactions of multi-reference character due to spin contamination, only for the addition of O_2 ($^3\Sigma_g^-$) to CF_3CHF radical path, we employed the procedure adopted by Maranzana *et al.* A series of constrained geometry optimizations at CASSCF(7,5)/cc-pVTZ level of theory were performed, where the distance between O and C2 (radical center in CH_3CHF) gradually changes, ensuring the minimal energy path of O_2 addition. This was followed by MRCI(7,5)/cc-pVTZ energy calculations at each point along the path. The active space for the multireference calculation was chosen to account for six valence electrons from four π-orbitals of O_2

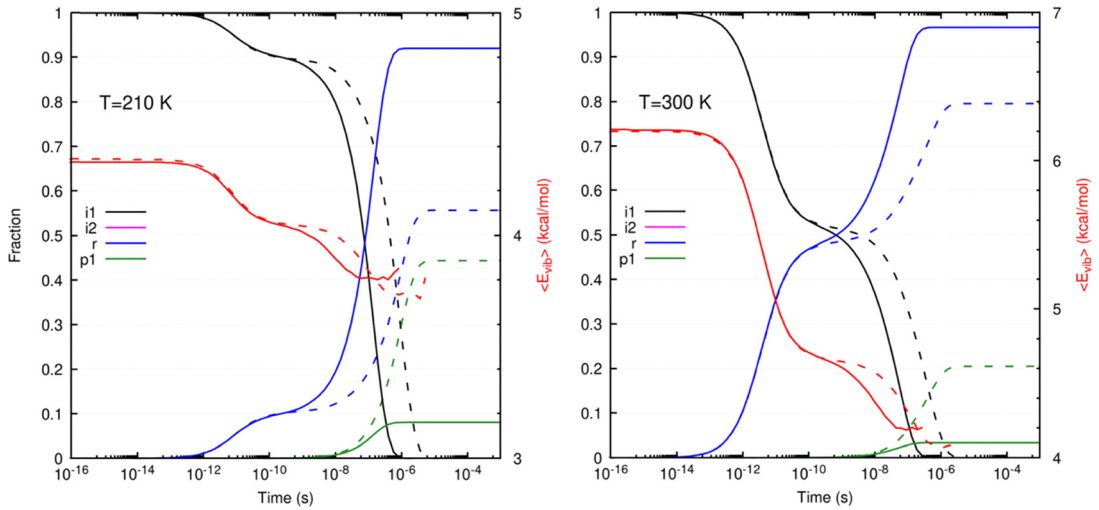

Fig. 3 Time evolution of the average vibrational energy of remaining **i1** (red line) and relative population of **r**, **i1**, **i2** and **p1**. Solid and dotted lines represent P = 1.0 atm and P = 0.1 atm, respectively. Left and right panels show results at T = 210 K and T = 300 K, respectively.

molecule and one unpaired electron and its orbital of the radical center. This procedure maintains the doublet spin state along the addition path, which is consistent with the rest of the potential energy profile in Fig. 4. The constrained optimized geometries and energies are used as input for the VTST calculation mentioned in the methods section.

O_2 ($^3\Sigma_g^-$) can add to the radical center (C2) of CF_3CHF *via* barrierless association to form the intermediate **i5** (CF_3CHFO_2 radical, −30.3 kcal mol^{-1}). This process is highly exothermic, releasing over 30 kcal mol^{-1} energy. **i5** could isomerize, where the terminal oxygen in CF_3CHFO_2 radical abstracts the hydrogen bonded to C2 and breaks the O–O bond to form **i6** (−67.9 kcal mol^{-1}), *via* a high transition state **ts-5-6** (12.3 kcal mol^{-1}). Note the potential energy released from O_2 addition ($CF_3CHF + O_2 \rightarrow$ **i5**) is smaller than the barrier height (**ts-5-6**) of further degradation. This observation supports the reported long-lifetime (*i.e.*, ∼100 s) of **i5** in the atmosphere.[1] **i6** is a vdW complex consisting of trifluoroacetyl fluoride (TFAF, CF_3CFO) and OH fragments. **i6** can either dissociate to TFAF and OH radical without a transition state (**p6**, TFAF + OH, −65.6 kcal mol^{-1}) or isomerize *via* a transition state **ts-6-8** (−60.4 kcal mol^{-1}), where the OH radical makes a bond with the carbonyl carbon (C2) to form **i8** (−78.6 kcal mol^{-1}). It is interesting to note that from the perspective of HFC-134a, OH radical acts as the catalyst in the overall reaction:

$$CF_3CFH_2 + O_2 \xrightarrow{^{\bullet}OH} CF_3CFO + H_2O$$

Similar to how **i8** is formed, the other pathway of **i6** involves the OH radical making a bond with the carbonyl carbon *via* a

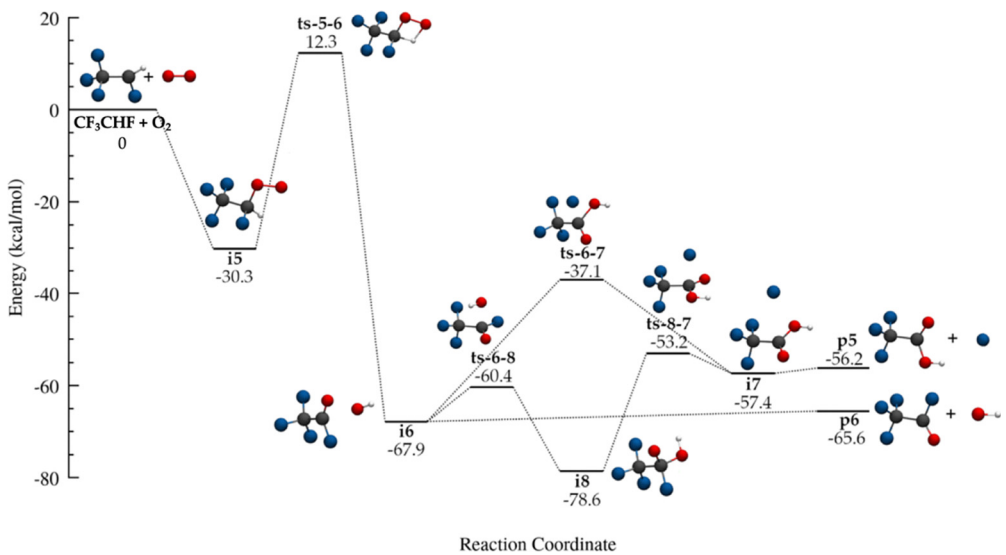

Fig. 4 Potential energy profile of the CF3CHF radical + O2 ($3\Sigma_g^-$) reaction computed with CCSD(T)-F12/cc-pVTZ-F12//M06-2X-D3/cc-pVTZ level of theory with ZPE included. The atoms are represented as black (C), blue (F), red (O) and white (H).

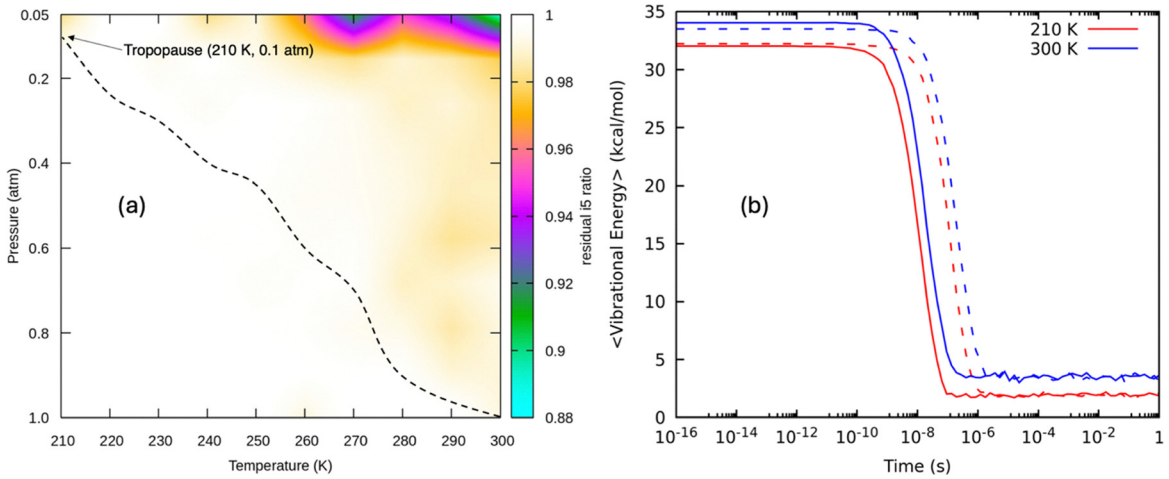

Fig. 5 (a) Residual **i5** as a function of temperature and pressure. The dotted line represents the temperature and pressure trend with altitude increase in the troposphere starting from T = 300 K and P = 1 atm at sea level to T = 210 K and P = 0.1 atm at 18 km. (b) Average vibrational energy, excluding ZPE contributions, over time of **i5** at two temperatures (red, 210 K; blue, 300 K) and pressures (solid, 1.0 atm; dashed, 0.1 atm).

transition state **ts-6-7** (−37.1 kcal mol^{-1}), but **ts-6-7** leads to the elimination of the F atom and forms trifluoroacetic acid (TFA, CF_3COOH), **p5** (TFA + F, −56.2 kcal mol^{-1}). **i8** can also lead to **p5** *via* **ts-8-7** (−53.2 kcal mol^{-1}) following the formation of **i7** (−57.4 kcal mol^{-1}) due to the elimination of the F atom from C2.

Although the reported reaction pathway of forming TFA from HFC-134a degradation has been identified in our research, the high energy barrier (**ts-5-6**) opens the question of how relevant it is under atmospheric conditions.[13] Therefore, kinetic study was carried out for **i5**, which is formed from barrierless association of CH_3CHF radical (its formation has been confirmed in the previous section) and O_2 ($^3\Sigma_g^-$). The LJ parameters for CH_3CHF radical (same as HFC-134a) and O_2 (σ = 3.39 Å, ε = 121.7 K) were used to estimate the LJ parameters for **i5**, **i6**, **i7** and **i8** using the aforementioned combination expressions.[63,64] The master equation simulations were initiated from **i5** at different temperatures (210–300 K) and pressures (0.1–1 atm). Fig. 5(a) shows that until 0.001 second, well over 90% of the species remain as **i5** across all temperature and pressure ranges. For those **i5** that dissociated, they form **p1** + O_2. The master equation simulations were extended to 1 s for extreme conditions, (*e.g.*, 300 K and 1.0 atm; 210 K and 0.1 atm), and the results are shown in Fig. 5(b). Here we reiterate that at the beginning of the simulation (t = 0), the vibrational energy (E_P) of **i5** includes the ZPE (E_{ZPE}, 26.9 kcal mol^{-1}), the thermal vibrational excitation sampled at its corresponding temperature (E_T), and the potential energy release from the association of CH_3CHF radical and O_2 (E_P, 30.3 kcal mol^{-1}). As the figure shows, E_P is quickly depleted as the collision with N_2 bath takes place. At this point, thermal stabilized **i5** is not expected to cross the high barrier **ts-5-6** and further degrade to TFA in large quantity.

Another potential degradation product of HFC-134a, TFAF (**p6**, CH_3CFO) is also identified in Fig. 4. TFAF has been reported to undergo hydrolysis reaction to form TFA in the water droplets or ice crystals in the atmosphere and then is brought to the ground with precipitation.[65] Although making TFAF relies on forming **i6**, which has been shown to be infeasible under atmospheric conditions for HFC-134a, we studied the energetics of the hydrolysis of TFAF in the gas phase. TFAF could potentially be formed from other sources and is a species that have been proposed by atmospheric modeling.[15,23] The earliest *ab initio* potential energy profile study for the gas-phase hydrolysis of TFAF has been reported by Francisco, where a high reaction barrier of 35.5 kcal mol^{-1} leads to TFA + HF formation.[66] In the present study, the potential energy profile for the hydrolysis step at singlet state is extended to study other possible reaction channels and is shown in Fig. 6.

The association between TFAF and H_2O is slightly exothermic and leads to a vdW complex (**i9**, −3.6 kcal mol^{-1}). **i9** connects to two dissociation pathways. First, it can go through a transition state (**ts-9-10**, 32.3 kcal mol^{-1}) where the oxygen atom in H_2O forms a bond with the carbonyl C atom of TFAF. Simultaneously, the O–H and C (carbonyl)–F bonds are broken, leading to the forming of a vdW complex **i10**, −9.9 kcal mol^{-1}. **i10** can dissociate to form TFA and HF, **p7** (−7.9 kcal mol^{-1}) without a transition state. The second pathway goes through a much higher transition state, **ts-9-11** (79.0 kcal mol^{-1}), where the H_2O molecule attacking the carbonyl carbon in TFAF leads to the C–C bond breaking. The H_2O molecule simultaneously splits – the H atom is transferred to the C1 atom of the TFAF, forming trifluoromethane (CHF_3), while the OH radical is transferred to the C2 atom of TFAF, forming fluoroacetic acid (FCOOH) – and forms the vdW complex **i11** (−12.6 kcal mol^{-1}). **i11** can dissociate to form CHF_3 and FCOOH, **p8** (−10.1 kcal mol^{-1}) without a transition state. The higher barriers associated in formatting **p7** and **p8** suggest that TFAF is stable in the gas phase under atmospheric conditions.

Degradation of i5 with other atmospheric radicals

Our kinetics study shows that CF_3CHFO_2 radical (**i5**) is collision-stabilized under atmospheric conditions. Combining

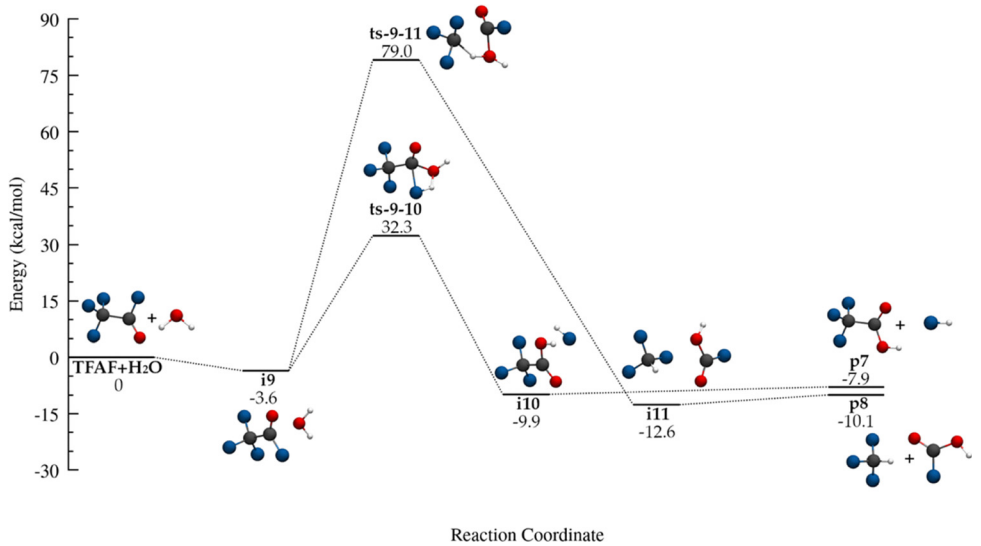

Fig. 6 Potential energy profile of the CF_3CFO + H_2O reaction computed with CCSD(T)-F12/cc-pVTZ-F12//M06-2X-D3/cc-pVTZ level of theory with ZPE included. The atoms are represented as black (C), blue (F), red (O) and white (H).

with the observed ~100 s lifetime of **i5**, it is of interest to understand **i5**'s reactivity with reactive radicals such as NO, HO_2, and NO_2. Although the abundances of these radicals (10^8 to 10^9 molecules cm^{-3}) largely depend on the altitude and locations, there have been reports on their rate constants reacting with **i5** in the range of 10^{-11} to 10^{-12} cm^3 $molecule^{-1}$ s^{-1}.

NO radical addition to CF_3CHFO_2 radical

The NO radical can add barrierlessly to **i5** intermediate with the N atom forming a Sigma bond with the terminal O atom of **i5** to form an intermediate **i12** (−27.0 kcal mol^{-1}). The reaction pathways associated with the NO radical addition at singlet state are outlined in Fig. 7(a). The O–O bond dissociation leads to the three decomposition pathways from **i12**. First, the oxygen atom in the departing NO_2 group can abstract the hydrogen atom *via* **ts-12-13** (2.8 kcal mol^{-1}), forming a vdW complex **i13** (−85.0 kcal mol^{-1}) that can dissociate to form TFAF and HONO (**p9**, −82.6 kcal mol^{-1}). The second pathway is similar to the first, except that the hydrogen atom was abstracted by the nitrogen atom of the NO_2 departing group *via* **ts-12-14** (−1.4 kcal mol^{-1}), which leads to the formation of a vdW complex **i14** (−79.5 kcal mol^{-1}). **i14** can further dissociate to form CF_3CFO and HNO_2 (**p10**, −74.9 kcal mol^{-1}) without a barrier. Both **p9** and **p10** include TFAF but differ in structural isomers of HNO_2. In the third pathway, the departing NO_2 group pivots and forms a new N–O Sigma bond *via* **ts-12-15** (0.6 kcal mol^{-1}), leading to a vdW complex, **i15** (−50.2 kcal mol^{-1}). **i15** can dissociate to form CF_3CHFO and NO_2 (**p11**, −18.6 kcal mol^{-1}). Judging by Fig. 7, the potential energy released from NO addition (CF_3CHFO_2 + NO → **i12**) is 27.0 kcal mol^{-1}, which is enough to cross **ts-12-14** and eventually form TFAF + HNO_2 (**p10**). Nonetheless, the other two barriers (**ts-12-13** and **ts-12-15**) are not much higher and could be competitive reactions. Hence a kinetic study of **i12** is carried out at atmospheric temperatures and pressures.

The LJ parameters from the master equation simulation of **i12**, **i13**, **i14**, **i15** and **i16** are derived by combining the LJ parameters of **i5** (σ = 3.61 Å, ε = 130.5 K) and NO radical (σ = 3.49 Å, ε = 117.0 K) using the combining rules described in the previous section.[67] The master equation simulations were initiated from **i12** at different temperatures (210–300 K) and pressures (0.1–1.0 atm) mimicking atmospheric conditions. The results are shown in Fig. 7(b) and (c). We note the simulations were extended up until 1 s but yielded no significant change in the results. Similar to the previous master equation simulations, the vibrational energy of **i12** at t = 0 is the sum of thermal vibrational excitation energy at a corresponding temperature and potential energy released in the formation of **i12** (27.0 kcal mol^{-1}) on top of the ZPE energy of **i12** (E_{ZPE}, 32.3 kcal mol^{-1}). Less than 2% of **i12** forms **i5** + NO reactants mostly at pressures less than 0.1 atm and around 300 K, far from atmospheric conditions. The remaining **i12** is collisionally stabilized as the collisions with N_2 bath gas takes place. Although **ts-12-13**, **ts-12-14**, **ts-12-15** and **i5** + NO are close in energy, only dissociation to **i5** + NO is observed due to large configurational change in the transition states as compared to **i12**. It would be of interest to perform unimolecular *ab initio* molecular dynamics simulations to further confirm the fate of **i12**, as this reaction would be non-RRKM. Nonetheless, with the evidence gathered so far, NO radical addition to CF_3CHFO_2 is not likely leading to the formation of TFAF or TFA.

HO_2 radical addition to CF_3CHFO_2 radical

The HO_2 radical adds barrierlessly to the β oxygen of the peroxy radical **i5** to form an intermediate **i17** (−16.9 kcal mol^{-1}). The HO_2 addition reaction potential energy profile at singlet state is outlined Fig. 8(a). Three product channels have been identified from the degradation of **i17**. First, the hydrogen atom in HO_2 radical is transferred to the fluorine atom on C2 which breaks

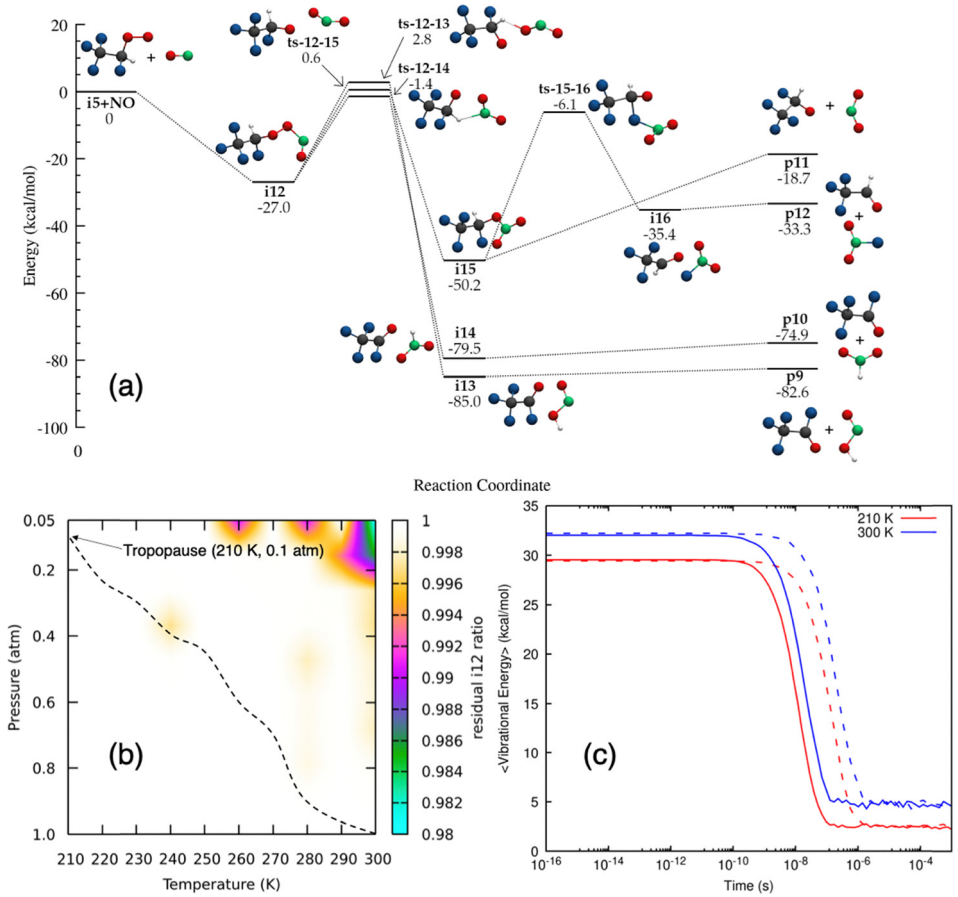

Fig. 7 (a) Potential energy profile of the CF_3CHFO_2 radical + NO reaction computed with CCSD(T)-F12/cc-pVTZ-F12//M06-2X-D3/cc-pVTZ level of theory with ZPE included. The atoms are represented as black (C), blue (F), red (O), green (N) and white (H). (b) Residual **i12** as a function of temperature and pressure. The dotted line represents the temperature and pressure trend with altitude increase in the troposphere starting from T = 300 K and P = 1 atm at sea level to T = 210 K and P = 0.1 atm at 18 km (tropopause). (c) Time evolution of the average vibrational energy of **i12** at T = 210 (red) and 300 K (blue). The solid and dotted lines represent P = 1.0 atm and P = 0.1 atm, respectively. ZPE has been subtracted from the vibrational energy shown in the figure.

the C2–F bond to form HF. This simultaneously leads to the bond cleavage between α oxygen and β oxygen, forming O_3 molecule *via* **ts-17-18** (11.8 kcal mol^{-1}). HF, O_3, and the remaining molecule (TFAF) form a loosely bond, vdW complex, **i18** (−22.4 kcal mol^{-1}). O_3 can break off from this complex, leaving a vdW complex of TFAF – HF behind (**p13**, −16.1 kcal mol^{-1}). Second, the hydrogen atom from the HO_2 radical could transit from the δ oxygen to the β oxygen *via* **ts-17-19** (18.1 kcal mol^{-1}), subsequently breaking the bond between the β oxygen and γ oxygen and forming a vdW complex **i19** (−44.9 kcal mol^{-1}). **i19** can dissociates to form $CF_3CHFOOH$ and $^3O_2$ without a transition state (**p14**, −44.0 kcal mol^{-1}). The last pathway features the simultaneous bond cleavage between β oxygen and γ oxygen and H atom abstraction from C2 *via* **ts-17-20** (17.9 kcal mol^{-1}) to form a vdW complex **i20** (−11.7 kcal mol^{-1}). **i20** can dissociate to form CF_3CFO_2 and H_2O_2 (**p15**, −2.4 kcal mol^{-1}) without a transition state. Although the addition of HO_2 radical to **i5** could lead to the formation of TFAF, it seems unlikely judging from the barriers associated with these pathways. Nonetheless, the master equation simulation was still performed.

The LJ parameters from the master equation simulation of **i17**, **i18**, **i19** and **i20** are derived by combining the LJ parameters of **i5** (σ = 3.61 Å, ε = 130.5 K) and HO_2 radical (σ = 4.19 Å, ε = 289.3 K) using the combining rules described in the previous section.[68] The master equation simulations were initiated from **i17** at different temperatures (210–300 K) and pressures (0.1–1.0 atm) mimicking atmospheric conditions. Fig. 8(b) presents the fraction of residual **i17** at the end of the simulation, while Fig. 8(c) shows the average vibrational energy of surviving **i17** over time at two extreme temperatures (210 K and 300 K) and pressures (0.1 atm and 1.0 atm). The vibrational energy (E_{vib}) of **i17** at t = 0 is the sum of thermal vibrational excitation energy (E_T) at a corresponding temperature and potential energy (E_P) released in the formation of **i17** (16.9 kcal mol^{-1}) on top of the ZPE energy of **i17** (E_{ZPE}, 39.2 kcal mol^{-1}). In the temperature regime of ≥270 K, up to 16% of vibrationally excited **i17** dissociate back to the reactant (**i5** + HO_2) and the rest are stabilized by the collision with N_2 bath. Whereas in the temperature range of 210 – 270 K, almost all of **i17** remain unreactive. A large fraction of vibrationally

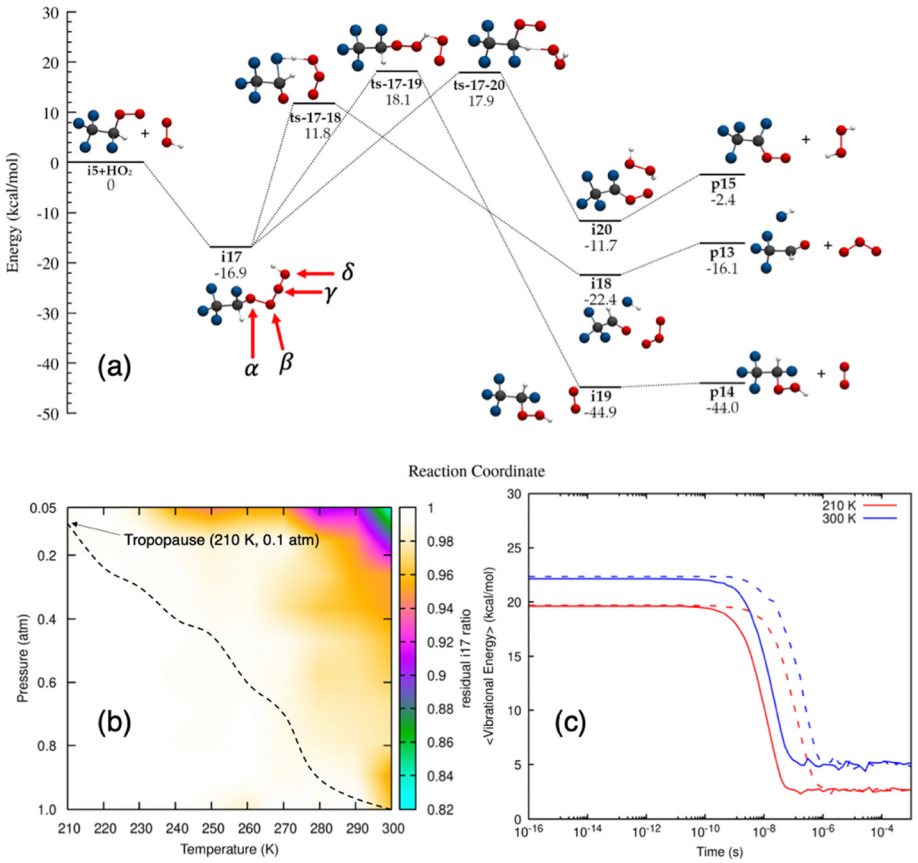

Fig. 8 (a) Potential energy profile of the CF_3CHFO_2 radical + HO_2 reaction at CCSD(T)-F12/cc-pVTZ-F12//M06-2X-D3/cc-pVTZ level of theory with ZPE included. The atoms are represented as black (C), blue (F), red (O) and white (H). (b) Residual **i17** as a function of temperature and pressure. The dotted line represents the temperature and pressure trend with altitude increase in the troposphere starting from T = 300 K and P = 1 atm at sea level to T = 210 K and P = 0.1 atm at 18 km (tropopause). (c) Time evolution of the average vibrational energy of **i17** at T = 210 (red) and 300 K (blue). The solid and dotted lines represent P = 1.0 atm and P = 0.1 atm, respectively. ZPE has been subtracted from the vibrational energy shown in the figure.

excited **i17** is below the barrier threshold relative to **i17** *viz.* **ts-17-18** (28.7 kcal mol^{-1}), **ts-17-19** (35.0 kcal mol^{-1}) and **ts-17-20** (34.8 kcal mol^{-1}) whereas the **i5** + HO_2 reactant channel is at 16.9 kcal mol^{-1}, thus making the reactant channel more easily accessible.

NO_2 radical addition to CF_3CHFO_2 radical

The potential energy profile at singlet state of the NO_2 radical addition to **i5** is presented in Fig. 9(a). In an exothermic process, the NO_2 radical forms a N–O bond with **i5** to form **i21** (−24.6 kcal mol^{-1}). **i21** can isomerize to **i22** (−0.2 kcal mol^{-1}) undergoing the 'nitro-to-nitrite' reaction *via* **ts-21-22** (6.4 kcal mol^{-1}). Similar 'nitro' to 'nitrite' linkage isomerization has been observed in unimolecular decomposition of energetic materials such as FOX-7.[69,70] The isomerization of **i22** to **i25** (−50.1 kcal mol^{-1}) involves a series of bond breaking and forming process. The bond between β oxygen and γ oxygen dissociates, where the NO_2 fragment pivots and forms a C2–O bond. As a result, the hydrogen atom bonded with C2 transits to β oxygen. **ts-22-25** is identified to have the highest energy barrier relative to all other stationary points in the addition reaction of **i5**. **i25** undergoes further isomerization *via* 90° dihedral angle rotation of O–N–O–C2, directing the NO moiety pointing towards the fluorine atom attached to C2. The NO fragment dissociates and abstracts the F atom to form **i26** (−46.2 kcal mol^{-1}). The vdW complex **i26** can either dissociate barrierlessly to form nitrosyl fluoride (NOF) and trifluoroperacetic acid (CF_3COOOH) (**p18**, −41.0 kcal mol^{-1}), or the vdW complex could isomerize *via* **ts-26-27** (−30.1 kcal mol^{-1}) to form **i27** (−57.4 kcal mol^{-1}). The isomerization step *via* **ts-26-27** involves the fluorine atom (dissociated from the NOF fragment) abstracting the hydrogen atom from the β oxygen atom in CF_3COOOH. **i27** can either dissociate to form nitrosyl trifluoroperoxyacetate ($CF_3C(O)OONO$) along with HF (**p19**, −55.1 kcal mol^{-1}) without a transition state or isomerize *via* **ts-27-28** (−17.8 kcal mol^{-1}) to form a vdW complex, **i28** (−55.4 kcal mol^{-1}). Along this isomerization path, the fluorine atom of the HF fragment recombines with the carbonyl carbon (C2) and breaks the α oxygen–C2 bond. The leftover hydrogen atom and OONO fragment forms nitrosyl-*O*-hydroxide (HO-ONO). **i28** can barrierlessly dissociate to form TFAF and HO-ONO (**p20**, −52.8 kcal mol^{-1}) without a transition state. The NO_2 group departing as a result of β oxygen–N bond dissociation in **i21** can also lead to the abstraction of H atom from C2 *via*

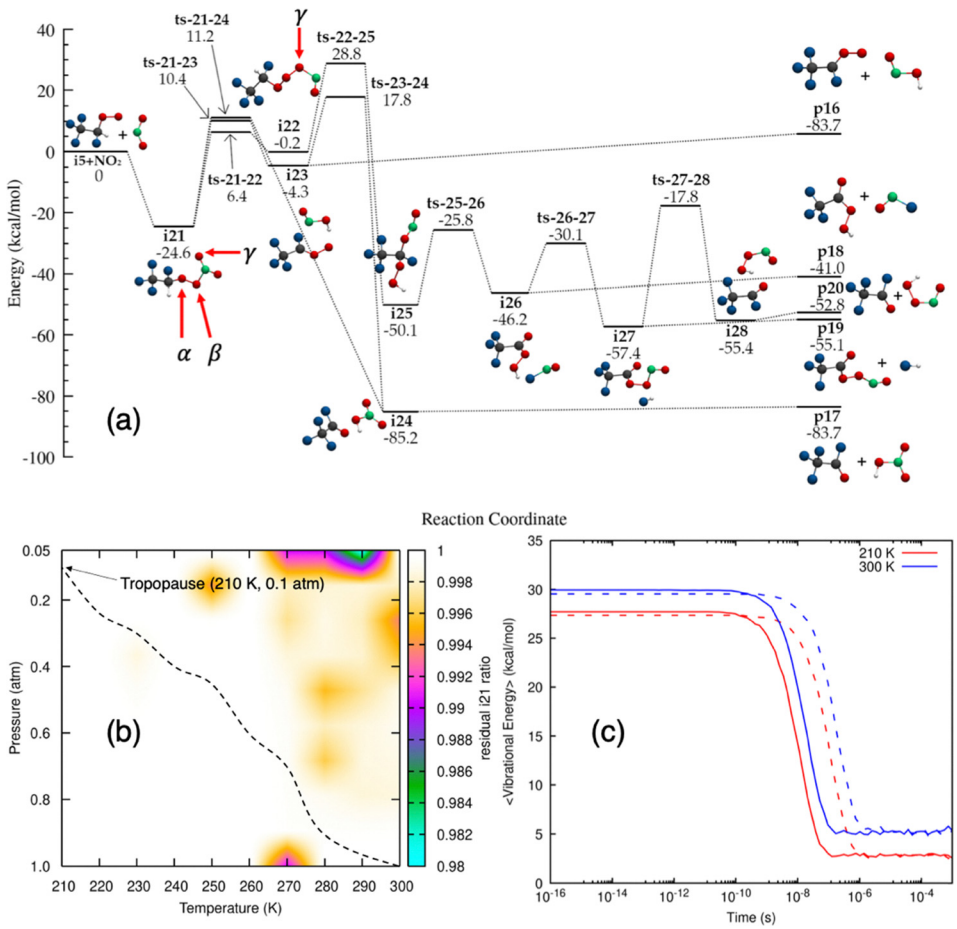

Fig. 9 (a) Potential energy profile of the CF_3CHFO_2 radical + NO_2 reaction at CCSD(T)-F12/cc-pVTZ-F12//M06-2X-D3/cc-pVTZ level of theory with ZPE included. The atoms are represented as black (C), blue (F), red (O), green (N) and white (H). Structures of the transition states can be found in the SI. (b) Residual **i21** as a function of temperature and pressure. The dotted line represents the temperature and pressure trend with altitude increase in the troposphere starting from T = 300 K and P = 1 atm at sea level to T = 210 K and P = 0.1 atm at 18 km (tropopause). (c) Time evolution of the average vibrational energy of **i21** at T = 210 (red) and 300 K (blue). The solid and dotted lines represent P = 1.0 atm and P = 0.1 atm, respectively. ZPE has been subtracted from the vibrational energy shown in the figure.

ts-21-23 (10.4 kcal mol^{-1}) and form a vdW complex, **i23** (−4.3 kcal mol^{-1}). **i23** can either dissociate to form CF_3CFOO + HONO (**p16**, 5.9 kcal mol^{-1}) without a transition state or isomerize to another vdW complex **i24** *via* **ts-23-24** (17.8 kcal mol^{-1}). In the isomerization pathway, the N atom from the HONO fragment abstracts the β oxygen atom and forms the HNO_3 fragment. **i24** could also be directly formed from **i21**, followed by a bond cleavage between the α and β oxygen and a hydrogen abstraction. **i24** can dissociate to TFAF and HNO_3 without a transition state.

The LJ parameters for all intermediates in Fig. 9(a) are derived by combining the LJ parameters of **i5** (σ = 3.61 Å, ε = 130.5 K) and NO_2 radical (σ = 4.68 Å, ε = 146 K) using the combining rules described in the previous section.[71] The master equation simulations were initiated from **i21** at different temperatures (210–300 K) and pressures (0.1–1.0 atm) mimicking atmospheric conditions. Fig. 9(b) presents the fraction of residual **i21** by the end of the simulation, while Fig. 9(c) shows the average vibrational energy of surviving **i21** over time. The vibrational energy of **i21** at t = 0 is the sum of thermal vibrational excitation energy at a corresponding temperature and potential energy released in the formation of **i21** (24.6 kcal mol^{-1}) on top of the ZPE energy of **i21** (E_{ZPE}, 36.1 kcal mol^{-1}). Similar to the results obtained for HO_2 addition reaction, the higher temperature regime (≥270 K) has up to 2% of **i21** dissociating back to reactants (**i5** + NO_2). The remaining fraction of **i21** is collisionally stabilized by N_2 bath gas. Therefore, **i5** reacting NO_2 is not likely to be a major source of TFAF or TFA in the atmosphere either.

Conclusions

This study explores the formation of TFA from HFC-134a under atmospheric conditions. 20 product channels have been identified, out of which two involve forming TFA and five involve forming TFAF, a key precursor of TFA reported in the literature.[65] However, master equation simulations reveal that under atmospheric conditions, although HFC-134a can react with OH radical and form an intermediate, the further

evolution of this intermediate to TFA and TFAF seems to be forbidden. Once again, the radicals and reaction pathways studied in this manuscript are the first attempt of characterizing the energetics of the reaction pathways that have already been proposed, but the results cast doubt on the relevance of these pathways in forming TFA. However, this work should not lead to the conclusion that HFC-134a is not responsible for TFAs in the atmosphere, as there are a large number of radicals in the atmosphere, leading to an astronomical number of potential reaction pathways. Potential reactions also include self-reactions of CF_3CHFO_2 (**i5**) and other radicals such as **i12**, **i17** and **i21**. Interestingly, aerosols could play a role in alternating reaction pathways of these molecules, as seen in the recent atmospheric chemistry study of organosulfate molecules.[72] Further, photochemistry could play an important role in the formation of TFA, as the UV absorption cross section for CF_3CHFO_2 (220 nm, gas-phase, 298 K) is reported to be $(5.34 \pm 0.2) \times 10^{-18}$ cm^2 molecule^{-1}.[73,74] Another potential factor that has not be explored is the role that ice grains might play.[75]

Author contributions

A. V. and R. S. designed the research; A. V. performed the calculations and analyzed the results; A. V. wrote the manuscript; K. F., Y. L., R. I. K., and R. S. edited the manuscript. R. S. supervised the research.

Conflicts of interest

There are no conflicts to declare.

Data availability

All the data are included in the manuscript and/or the SI. Supplementary Information is available. See DOI: https://doi.org/10.1039/d5cp03359d.

Acknowledgements

This study was funded through the NSF award, 2330175, Center: NSF Engineering Research Center for Environmentally Applied Refrigerant Technology Hub. The authors acknowledge the Information and Technology Services (ITS) from the University of Hawai'i, Manoa.

References

1 Scientific Assessment of Stratospheric Ozone, National Aeronautics and Space Administration, 1989.
2 Ozone Secretariat to the Vienna Convention for the Protection of the Ozone Layer and the Montreal Protocol on Substances that Deplete the Ozone Layer, Ed., Handbook for the international treaties for the protection of the ozone layer: the Vienna Convention (1985); the Montreal Protocol (1987), UNEP, Ozone Secretariat, Nairobi, 6th ed., 2003.
3 L. M. Carlson, M. Angrish, A. V. Shirke, E. G. Radke, B. Schulz, A. Kraft, R. Judson, G. Patlewicz, R. Blain, C. Lin, N. Vetter, C. Lemeris, P. Hartman, H. Hubbard, X. Arzuaga, A. Davis, L. V. Dishaw, I. L. Druwe, H. Hollinger, R. Jones, J. P. Kaiser, L. Lizarraga, P. D. Noyes, M. Taylor, A. J. Shapiro, A. J. Williams and K. A. Thayer, *Environ. Health Perspect.*, 2022, **130**, 056001.
4 D. J. Bowden, S. L. Clegg and P. Brimblecombe, *Chemosphere*, 1996, **32**, 405–420.
5 A. L. Henne and C. J. Fox, *J. Am. Chem. Soc.*, 1951, **73**, 2323–2325.
6 M. D. Hurley, M. P. Sulbaek Andersen, T. J. Wallington, D. A. Ellis, J. W. Martin and S. A. Mabury, *J. Phys. Chem. A*, 2004, **108**, 615–620.
7 T. E. Møgelberg, O. J. Nielsen, J. Sehested, T. J. Wallington and M. D. Hurley, *Chem. Phys. Lett.*, 1994, **226**, 171–177.
8 M. de los A. Garavagno, R. Holland, M. A. H. Khan, A. J. Orr-Ewing and D. E. Shallcross, *Sustainability*, 2024, **16**, 2382.
9 M. O. McLinden and M. L. Huber, *J. Chem. Eng. Data*, 2020, **65**, 4176–4193.
10 B. Xiang, P. K. Patra, S. A. Montzka, S. M. Miller, J. W. Elkins, F. L. Moore, E. L. Atlas, B. R. Miller, R. F. Weiss, R. G. Prinn and S. C. Wofsy, *Proc. Natl. Acad. Sci. U. S. A.*, 2014, **111**, 17379–17384.
11 S. G. Penoncello, R. T. Jacobsen, K. M. de Reuck, A. E. Elhassan, R. C. Williams and E. W. Lemmon, *Int. J. Thermophys.*, 1995, **16**, 781–790.
12 T. J. Wallington, M. D. Hurley, J. M. Fracheboud, J. J. Orlando, G. S. Tyndall, J. Sehested, T. E. Møgelberg and O. J. Nielsen, *J. Phys. Chem.*, 1996, **100**, 18116–18122.
13 J. Franklin, *Chemosphere*, 1993, **27**, 1565–1601.
14 J. C. Ball and T. J. Wellington, *Air Waste*, 1993, **43**, 1260–1262.
15 M. Kanakidou, F. Dentener and P. Crutzen, *J. Geophys. Res.: Atmos.*, 1995, **100**, 18781–18801.
16 J. Wu, J. W. Martin, Z. Zhai, K. Lu, L. Li, X. Fang, H. Jin, J. Hu and J. Zhang, *Environ. Sci. Technol.*, 2014, **48**, 3675–3681.
17 D. J. Luecken, R. L. Waterland, S. Papasavva, K. N. Taddonio, W. T. Hutzell, J. P. Rugh and S. O. Andersen, *Environ. Sci. Technol.*, 2010, **44**, 343–348.
18 A. Jordan and H. Frank, *Environ. Sci. Technol.*, 1999, **33**, 522–527.
19 A. Lindley, A. McCulloch and T. Vink, *Open J. Air Pollut.*, 2019, **8**, 81–95.
20 R. Holland, M. A. H. Khan, I. Driscoll, R. Chhantyal-Pun, R. G. Derwent, C. A. Taatjes, A. J. Orr-Ewing, C. J. Percival and D. E. Shallcross, *ACS Earth Space Chem.*, 2021, **5**, 849–857.
21 K. R. Solomon, G. J. M. Velders, S. R. Wilson, S. Madronich, J. Longstreth, P. J. Aucamp and J. F. Bornman, *J. Toxicol. Environ. Health, Part B*, 2016, **19**, 289–304.
22 Q. Wang, X. Wang and X. Ding, *Sci. Total Environ.*, 2014, **468–469**, 272–279.
23 V. R. Kotamarthi, J. M. Rodriguez, M. K. W. Ko, T. K. Tromp, N. D. Sze and M. J. Prather, *J. Geophys. Res.: Atmos.*, 1998, **103**, 5747–5758.

24 R. Liu, R. E. Huie and M. J. Kurylo, *J. Phys. Chem.*, 1990, **94**, 3247–3249.
25 T. J. Wallington and M. D. Hurley, *Chem. Phys. Lett.*, 1992, **189**, 437–442.
26 J. P. Sawerysyn, A. Talhaoui, B. Meriaux and P. Devolder, *Chem. Phys. Lett.*, 1992, **198**, 197–199.
27 G.-H. Leu and Y.-P. Lee, *J. Chin. Chem. Soc.*, 1994, **41**, 645–649.
28 T. Gierczak, R. Talukdar, G. L. Vaghjiani, E. R. Lovejoy and A. R. Ravishankara, *J. Geophys. Res.*, 1991, **96**, 5001–5011.
29 R. Warren, T. Gierczak and A. R. Ravishankara, *Chem. Phys. Lett.*, 1991, **183**, 403–409.
30 M. A. A. Clyne and P. M. Holt, *J. Chem. Soc., Faraday Trans. 2*, 1979, **75**, 582–591.
31 W. Braun, A. Fahr, R. Klein, M. J. Kurylo and R. E. Huie, *J. Geophys. Res.: Atmos.*, 1991, **96**, 13009–13015.
32 V. L. Orkin and V. G. Khamaganov, *J. Atmos. Chem.*, 1993, **16**, 157–167.
33 E. C. Tuazon and R. Atkinson, *J. Atmos. Chem.*, 1993, **16**, 301–312.
34 M. Matti Maricq, J. J. Szente and E. W. Kaiser, *Chem. Phys. Lett.*, 1992, **197**, 149–156.
35 T. J. Wallington and O. J. Nielsen, *Chem. Phys. Lett.*, 1991, **187**, 33–39.
36 R. Atkinson, NASA, Washington, Scientific Assessment of Stratospheric Ozone: 1989, Volume 2. Appendix: AFEAS Report.
37 R. V. Olkhov and I. W. M. Smith, *Phys. Chem. Chem. Phys.*, 2003, **5**, 3436–3442.
38 T. E. Møgelberg, O. J. Nielsen, J. Sehested, T. J. Wallington, M. D. Hurley and W. F. Schneider, *Chem. Phys. Lett.*, 1994, **225**, 375–380.
39 J. Sehested, T. Møgelberg, K. Fagerström, G. Mahmoud and T. J. Wallington, *Int. J. Chem. Kinet.*, 1997, **29**, 673–682.
40 M. Valiev, E. J. Bylaska, N. Govind, K. Kowalski, T. P. Straatsma, H. J. J. Van Dam, D. Wang, J. Nieplocha, E. Apra, T. L. Windus and W. A. De Jong, *Comput. Phys. Commun.*, 2010, **181**, 1477–1489.
41 Y. Zhao and D. G. Truhlar, *Theor. Chem. Acc.*, 2008, **120**, 215–241.
42 T. H. Dunning, *J. Chem. Phys.*, 1989, **90**, 1007–1023.
43 S. Grimme, J. Antony, S. Ehrlich and H. Krieg, *J. Chem. Phys.*, 2010, **132**, 154104.
44 S. Grimme, S. Ehrlich and L. Goerigk, *J. Comput. Chem.*, 2011, **32**, 1456–1465.
45 K. Fukui, *J. Phys. Chem.*, 1970, **74**, 4161–4163.
46 V. S. A. Bonfim, L. Baptista, D. A. B. Oliveira, D. E. Honda and A. C. F. Santos, *J. Mol. Model.*, 2022, **28**, 309.
47 A. D. Buettner, B. J. Dilday, R. A. Craigmile, M. C. Drummer, J. M. Standard and R. W. Quandt, *Phys. Chem. Chem. Phys.*, 2020, **22**, 24583–24599.
48 T. Zhang, C. Zhang, X. Ma and H. Quan, *Atmos. Environ.*, 2023, **294**, 119467.
49 R. R. Changmai and M. Sarma, *ACS Earth Space Chem.*, 2022, **6**, 1782–1792.
50 R. R. Changmai, S. R. Daimari, A. K. Yadav and M. Sarma, *Phys. Chem. Chem. Phys.*, 2024, **26**, 23363–23371.
51 Y. Shang and S. N. Luo, *Phys. Chem. Chem. Phys.*, 2024, **26**, 20167–20215.
52 C. Hättig, W. Klopper, A. Köhn and D. P. Tew, *Chem. Rev.*, 2012, **112**, 4–74.
53 L. Kong, F. A. Bischoff and E. F. Valeev, *Chem. Rev.*, 2012, **112**, 75–107.
54 K. Raghavachari, G. W. Trucks, J. A. Pople and M. Head-Gordon, *Chem. Phys. Lett.*, 1989, **157**, 479–483.
55 F. Neese, *Wiley Interdiscip. Rev.: Comput. Mol. Sci.*, 2012, **2**, 73–78.
56 Y. Shang, H. Ning, J. Shi and S.-N. Luo, *Proc. Combust. Inst.*, 2021, **38**, 853–860.
57 J. R. Barker, T. L. Nguyen, J. F. Stanton, C. Aieta, M. Ceotto, F. Gabas, G. Mandelli, T. J. D. Kumar, C. G. L. Li, L. L. Lohr, A. Maranzana, N. F. Ortiz, J. M. Preses, J. M. Simmie, J. A. Sonk and P. J. Stimac, *Multwell-2023.1 Software*, University of Michigan, Ann Arbor, 2023, https://multiwell.engin.umich.edu/.
58 K. A. Holbrook, M. J. Pilling and S. H. Robertson, *Unimolecular Reactions*, Wiley, 1996.
59 J. R. Barker, *Int. J. Chem. Kinet.*, 2001, **33**, 232–245.
60 J. R. Barker and N. F. Ortiz, *Int. J. Chem. Kinet.*, 2001, **33**, 246–261.
61 J. R. Barker, L. M. Yoder and K. D. King, *J. Phys. Chem. A*, 2001, **105**, 796–809.
62 W. F. Schneider, T. J. Wallington, J. R. Barker and E. A. Stahlberg, *Ber. Bunsenges. Phys. Chem.*, 1998, **102**, 1850–1856.
63 A. W. Jasper and J. A. Miller, *Combust. Flame*, 2014, **161**, 101–110.
64 P. K. Rai, A. Kumar and P. Kumar, *Phys. Chem. Chem. Phys.*, 2024, **26**, 22395–22402.
65 Ch George, J. Y. Saison, J. L. Ponche and Ph Mirabel, *J. Phys. Chem.*, 1994, **98**, 10857–10862.
66 J. S. Francisco, *J. Phys. Chem.*, 1992, **96**, 4894–4899.
67 H. Hippler, J. Troe and H. J. Wendelken, *J. Chem. Phys.*, 1983, **78**, 6709–6717.
68 A. Seif, L. R. Domingo and T. S. Ahmadi, *Comput. Theor. Chem.*, 2020, **1190**, 113010.
69 Y. Luo, C. Kang, R. Kaiser and R. Sun, *Phys. Chem. Chem. Phys.*, 2022, **24**, 26836–26847.
70 K. Yadav, Y. Luo, R. I. Kaiser and R. Sun, *Phys. Chem. Chem. Phys.*, 2024, **26**, 11395–11405.
71 J. Troe, *J. Chem. Phys.*, 1977, **66**, 4758–4775.
72 N. Tsona Tchinda, X. Lv, S. N. Tasheh, J. N. Ghogomu and L. Du, *Atmos. Chem. Phys.*, 2025, **25**, 8575–8590.
73 T. J. Wallington and O. J. Nielsen, *Chem. Phys. Lett.*, 1991, **187**, 33–39.
74 A. A. Jemi-Alade, P. D. Lightfoot and R. Lesclaux, *Chem. Phys. Lett.*, 1991, **179**, 119–124.
75 K. Mondal, S. Biswas, N. Melbourne, R. Sun and R. I. Kaiser, *Chem. Sci.*, 2025, **16**, 11039–11048.